

# NeuroRVQ: Multi-Scale EEG Tokenization for Generative Large Brainwave Models

Konstantinos Barmpas<sup>1,2</sup> Na Lee<sup>1,2</sup> Alexandros Koliousis<sup>3</sup> Yannis Panagakis<sup>2,4,5</sup> Dimitrios Adamos<sup>1,2</sup>  
Nikolaos Laskaris<sup>2,6</sup> Stefanos Zafeiriou<sup>1,2</sup>

## Abstract

Electroencephalography (EEG) captures neural activity across multiple temporal and spectral scales, yielding signals that are rich but complex for representation learning. EEG foundation models trained to predict masked signal tokens have shown promise in learning generalizable representations. However, their performance is hindered by signal tokenization: existing EEG signal tokenizers fail to preserve high-frequency dynamics, limiting their ability to reconstruct signals with high fidelity.

We introduce NEURORVQ, a scalable Large Brainwave Model (LBM) centered on a codebook-based tokenizer. Our tokenizer integrates: (i) multi-scale feature extraction modules that capture the full frequency neural spectrum; (ii) hierarchical residual vector quantization (RVQ) codebooks for high-resolution encoding; and (iii) a unit circle phase-aware loss for efficient training. This design enables efficient EEG compression while supporting accurate reconstruction across all frequency bands, leading to robust generative masked modeling. Our results demonstrate that NEURORVQ achieves a lower reconstruction error and outperforms existing LBMs on a variety of downstream tasks. Preliminary results on electromyography (EMG) and electrocardiogram (ECG) signal reconstruction suggest NEURORVQ’s potential to extend beyond EEG. More broadly, the NEURORVQ tokenizer establishes a strong prior for codebook-based general-purpose brainwave models, enabling advances in neural decoding, generative modeling and multimodal biosignal integration.

<sup>1</sup>Imperial College London <sup>2</sup>Cogitat Ltd. <sup>3</sup>Northeastern University London <sup>4</sup>National and Kapodistrian University of Athens <sup>5</sup>Archimedes Research Unit <sup>6</sup>Aristotle University of Thessaloniki. Correspondence to: Konstantinos Barmpas <konstantinos.barmpas16@imperial.ac.uk>.

Preprint. January 15, 2026.

## 1. Introduction

Brain-Computer Interface (BCI) systems enable direct communication between the brain and the external world by analyzing brainwaves recorded by electroencephalography (EEG) devices. EEG signals can represent the full spectrum of human experience, from sleep and emotions to movement. Decoding EEG signals is a fundamental component of BCIs that find application in various areas such as emotion recognition (Torres et al., 2020; Xu et al., 2018), epileptic seizure detection (Alkawadri, 2019; Djoufack Nkengfack et al., 2021) and robotic control (Irimia et al., 2012).

Brain activity unfolds across multiple frequency scales. Brainwave signals can be categorized into distinct frequency bands (Newson & Thiagarajan, 2018)—namely, delta (0.5–4 Hz), theta (4–8 Hz), alpha (8–13 Hz), beta (13–30 Hz) and gamma ( $> 30$  Hz)—each linked to specific cognitive and physiological states. For example, delta waves dominate during deep sleep, while alpha waves emerge during relaxing states (especially with closed eyes), but tend to decrease in amplitude during movement. Together, these bands provide a dynamic window into the brain’s activity and internal states. **EEG analysis must capture the multiscale structure of brainwaves, both slow and fast dynamics, to fully represent neural information.**

A range of techniques, from advanced signal processing to machine learning, have been employed for brainwave decoding. More recently, Large Brainwave Models (LBMs) offer strong generalization capabilities without relying on BCI task-specific data collection and model training. These models are typically trained using self-supervised masked learning: EEG signals are discretized into *tokens*; and, during training, tokens are intentionally masked so that models learn to reconstruct them. However, reconstructing raw EEG signals remains a significant challenge due to their inherently noisy and complex nature. Tokenizers must effectively capture spatio-temporal patterns (e.g., location of recording electrodes, time and frequency) to convert them into meaningful token representations. **Current tokenizers struggle to preserve the complete structural information (especially high frequency components) necessary for robust generative masked modeling.**

The key to unlocking foundation-scale masked modeling for EEG lies in the tokenizer:

A well-designed EEG tokenizer should not only compress continuous neural signals into discrete tokens but also enable faithful reconstruction of the original waveform across all important frequency scales.

In this work, we introduce NEURORVQ, an efficient and scalable LBM architecture. The main contribution of this work is its state-of-the-art tokenizer that:

- (1) captures multi-scale frequency features by applying temporal convolutions with varying kernel sizes, to effectively disentangle the underlying frequency components;
- (2) encodes hierarchical representations in Residual Vector Quantization (RVQ) codebooks, one per frequency scale, enabling us to learn and preserve the complex patterns necessary for high-fidelity signal reconstruction;
- (3) introduces a unit circle phase-aware training loss, grounded in strong signal processing principles, that captures both amplitude and wrapped phase information of the EEG signal via sine and cosine representations; and
- (4) can be adapted to other biosignal modalities by tuning kernel sizes for modality-specific frequencies and scaling RVQ codebooks to signal complexity.

We evaluate the efficacy of the NEURORVQ tokenizer by comparing its reconstruction capabilities to other state-of-the-art tokenizers. NEURORVQ foundation model achieves up to 15% higher performance on five BCI downstream tasks compared to other EEG foundation models, demonstrating the effectiveness of codebook-based modeling when codebooks faithfully reconstruct brain signals.

## 2. Background & Related Work

The roots of EEG analysis can be traced back to classical neuroscience methods, when handcrafted features such as Power Spectral Density (PSD) bands and Independent Component Analysis (ICA) were regarded standard (Bashashati et al., 2007; Handy, 2009; Rao, 2013; Nam et al., 2018; McFarland et al., 2006). Although these methods provided valuable insights into neural dynamics, they often failed to generalize due to high inter-subject variability, the noisy nature of EEG signal, and their limited capacity to capture the full complexity of brain activity.

The deep learning era marked a shift towards data-driven feature extraction: brainwave decoders such as EEGNet (Lawhern et al., 2018), EEGInception (Santamaría-Vázquez et al.,

2020), EEGConformer (Song et al., 2023) and Brainware-Scattering Net (Barmpas et al., 2023) reduced reliance on handcrafted features by automatically learning representations of brain activity. To address domain-specific challenges such as subject variability, researchers incorporated domain-specific knowledge into these architectures, such as subject-alignment to adjust feature representations (Bakas et al., 2022; Wei et al., 2022; Barmpas et al., 2024b). Despite these advances, most deep learning models remain limited: they require carefully labeled data and extensive task-specific training, hindering their ability to scale and generalize across diverse BCI tasks.

More recently, the success of large foundation models in natural language processing (Brown et al., 2020; Touvron et al., 2023) and computer vision (Mizrahi et al., 2023) has motivated their adoption in EEG decoding. LaBraM (Jiang et al., 2024), NeuroGPT (Cui et al., 2024), CBraMod (Wang et al., 2025), EEGPT (Wang et al., 2024) and BIOT (Yang et al., 2023) are examples of foundation models for brain signals, pretrained on massive unlabeled datasets using self-supervised signal reconstruction objectives. These models represent a promising direction for capturing complex signal patterns beyond task-specific methods. However, they face a fundamental bottleneck—signal tokenization.

Tokenization is critical for robust generative masked modeling, yet current tokenizers struggle to capture the full structure of brain signals. NeuroGPT relies on a deep backbone-based tokenizer while other models like BIOT and EEGPT on transformer-based tokenizers, which often learn entangled and redundant representations not optimized for reconstruction. As a result, the generated tokens lack the fidelity required for masked prediction. In contrast, LaBraM and more recently BrainOmni (Xiao et al., 2025) adopt a codebook-based approach to learn reconstructable neural tokens. However, while discrete codebook-based tokenizers work well in computer vision and audio, directly adopting them for brain signals has not yielded faithful signal reconstruction—until NEURORVQ.

## 3. NeuroRVQ Tokenizer

### 3.1. Model Architecture

NEURORVQ tokenizer is a specialized network designed to convert raw EEG signals into a sequence of compact and informative neural tokens. This transformation reduces the inherently high-dimensional and noisy nature of EEG into a structured lower-dimensional representation preserving essential temporal-spectral patterns. In doing so, the tokenizer provides a kind of “neural grammar” for brain activity.

Figure 1 illustrates the tokenizer architecture and processing flow. The input multi-variate timeseries is first segmented into EEG patches. These patches are encoded by the multi-

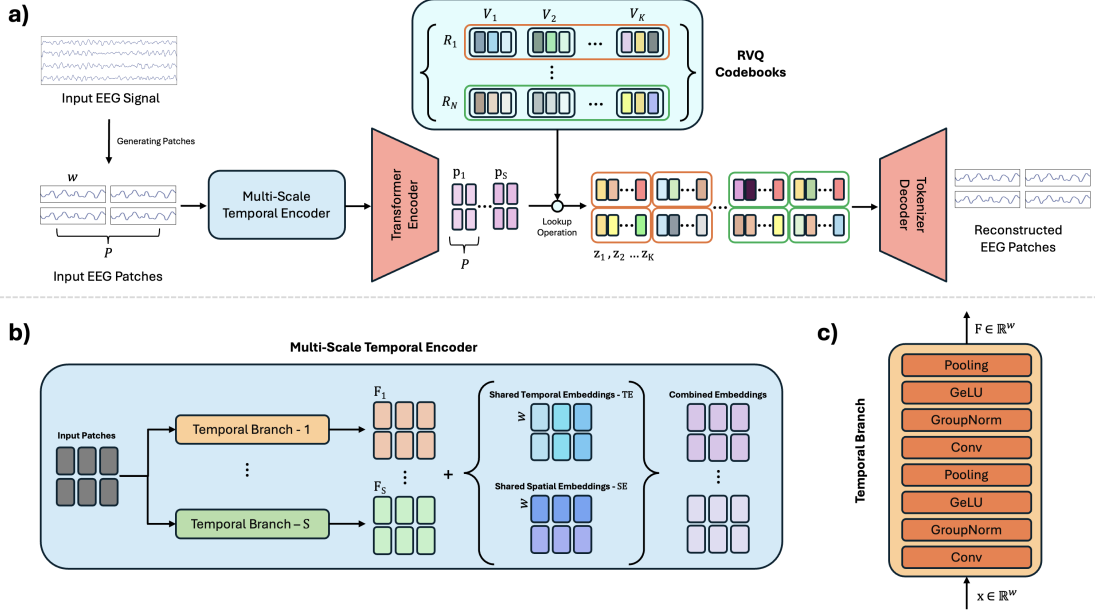


Figure 1. **a)** The NEURORVQ tokenizer model architecture; **b)** the multi-scale temporal encoder architecture; and **c)** the temporal branch architecture. The multi-scale temporal encoder extracts multi-scale temporal features that are passed to the transformer encoder. RVQ codebooks per temporal branch discretize the EEG patches into neural tokens. The tokenizer decoder reconstructs the EEG signal by using the Fourier spectrum.

scale temporal encoder, that captures features in multiple resolutions and are then combined via the transformer encoder. For each scale, RVQ codebooks discretize the embeddings into a sequence of neural tokens. Finally, these tokens from all scales are combined and passed through the tokenizer decoder to reconstruct the input EEG patches using the Fourier spectrum.

**Generating Patches:** Let  $X \in \mathbb{R}^{C \times T}$  denote the input EEG signal, where  $T$  is the number of time points and  $C$  is the number of electrodes. The signal is first segmented into temporal patches. To ensure that the tokenizer can accommodate EEG signals with arbitrary numbers of channels and variable durations, we adopt the following approach: during model pre-training, each input multi-variate EEG signal is represented by  $P$  patches of length  $w$  (corresponding to a 1-second time window). This results in a segmented input sample  $\mathbf{x} \in \mathbb{R}^{P \times w}$  which provides flexibility to handle heterogeneous EEG recordings and facilitates robust pre-training across diverse datasets.

**Multi-Scale Temporal Encoder:** The first step is to extract multi-scale temporal features from each input patch using an inception-style module with  $S$  distinct temporal scales. To achieve this, we apply 1-D temporal convolutions with varying kernel sizes  $K_{\text{temporal}_1}, K_{\text{temporal}_2}, \dots, K_{\text{temporal}_S}$ . Each temporal branch consists of the following sequence of operations: a 1-D convolution, followed by group normalization, GELU activation and pooling (this sequence of operations is

repeated twice). This design enables the network to capture temporal features at multiple scales resulting in  $S$  outputs  $F_1, F_2, \dots, F_S$  where  $F_i \in \mathbb{R}^w$  where  $w$  is the patch time window length.

**Transformer Encoder:** Since the tokenization of EEG signal takes place in a per-patch level, the vital temporal and spatial information is incorporated through the use of trainable temporal  $TE$  and spatial  $SE$  embeddings, each with embedding dimension  $w$ .  $SE = \{se_1, \dots, se_{|\mathcal{C}|}\}$  is indexed by the positions of the patches' electrodes within a list of all electrodes in the entire pre-training database  $\mathcal{C}$  and  $TE = \{te_1, \dots, te_P\}$  since each input consists of  $P$  patches of length  $w$ . These embeddings are added to the extracted multi-scale features  $F_1, F_2, \dots, F_S$  and are shared across all  $S$  temporal branches. The combined embeddings of each temporal branch are then passed through a series of shared transformer layers (Vaswani et al., 2023) resulting in the multi-scale patch representations  $\mathbf{p}_1, \mathbf{p}_2, \dots, \mathbf{p}_S \in \mathbb{R}^D$ . The shared transformer layers have incorporated the modification of Dehghani et al. (2023).

**RVQ Codebook:** To efficiently discretize the multi-scale patch representations  $\mathbf{p}_1, \mathbf{p}_2, \dots, \mathbf{p}_S$  while preserving fine-grained information of the EEG signal, we use  $S$  Residual Vector Quantization (RVQ) codebooks (Gray, 1984). For each temporal branch, the RVQ codebook  $\mathcal{R}$  is defined as:

$$\mathcal{R} = \{\mathcal{V}_i | i = 1, \dots, N\} \quad (1)$$

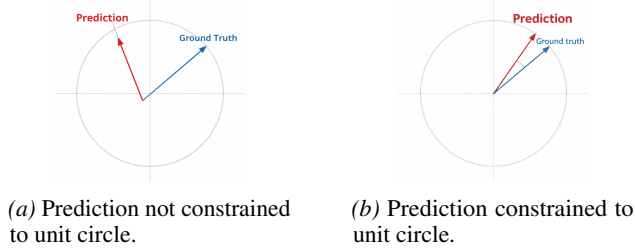


Figure 2. Comparison of phase modeling approaches: (a) Independent MSE can produce invalid predictions (b) Unit-circle-aware loss enforces valid phase angles.

where  $\mathcal{V}_i$  is a single codebook of neural tokens defined as:

$$\mathcal{V}_i = \{\mathbf{v}_j | j = 1, \dots, K\} \in \mathbb{R}^{K \times D} \quad (2)$$

where  $K$  is the number of discrete neural tokens and  $D$  is the dimensionality of each token. The discretization of the patch representations is performed iteratively. For each  $\mathcal{R}$ , at step 1, a quantizer maps each patch representation  $\mathbf{p}^1$  to its corresponding neural token  $\mathbf{v}^1 \in \mathcal{V}_1$ . Specifically, for each patch, the quantizer selects the nearest neighbor  $\mathbf{z}_1$  from the codebook  $\mathcal{V}_1$ :

$$\mathbf{z}_1 = \arg \min_{\mathbf{v}^1 \in \mathcal{V}_1} \|l_2(\mathbf{p}^1) - l_2(\mathbf{v}^1)\| \quad (3)$$

At each next step  $i + 1$ , the residual patch representation  $\mathbf{p}^{i+1}$  for the next codebook  $\mathcal{V}_{i+1}$  is updated by subtracting the selected token  $\mathbf{z}_i$ :

$$\mathbf{p}^{i+1} = \mathbf{p}^i - \mathbf{z}_i \quad (4)$$

This process is repeated for all  $N$  codebooks, producing a sequence of tokens  $\mathbf{z}_1, \mathbf{z}_2, \dots, \mathbf{z}_N$  for each temporal branch separately. The final reconstructed patch representations  $\hat{\mathbf{p}}$  is obtained by summing the contributions of all selected tokens  $\mathbf{z}_1, \mathbf{z}_2, \dots, \mathbf{z}_N$ :

$$\hat{\mathbf{p}} = \sum_{i=1}^N \mathbf{z}_i \quad (5)$$

At the end of this module, we have  $\hat{\mathbf{p}}_1, \hat{\mathbf{p}}_2, \dots, \hat{\mathbf{p}}_S$  corresponding to the  $S$  temporal branches.

**Tokenizer Decoder:** The purpose of the decoder module (a series shared transformer layers followed by prediction heads) is to reconstruct the original signal information based on the learned codebook tokens. Directly reconstructing raw EEG signals has been shown to yield unstable training and poor performance, due to the inherently noisy and high-dimensional nature of EEG. Following the strategy of

LaBraM (Jiang et al., 2024), we leverage the Fourier spectrum (more specifically the phase  $\phi$  and spectral amplitude  $A$ ) as a more structured target for reconstruction.

### 3.2. Tokenizer Training

Reconstructing the phase  $\phi$  directly with mean squared error (MSE) is suboptimal due to the periodic nature of the Fourier phase (see Appendix A). To address this, our architecture replaces raw phase reconstruction with a sine/cosine phase representation and we predict the  $\sin \hat{\phi}$  and  $\cos \hat{\phi}$ , which are smooth, continuous and better suited as loss terms. For the amplitude component, rather than reconstructing raw spectral magnitudes  $A$ , we operate in the log-amplitude domain  $\log(1 + A)$ . This logarithmic scaling compresses the large dynamic range of EEG spectra and places relatively greater emphasis on reconstructing high-frequency components, a key weakness in existing tokenizers. Therefore, the tokenizer decoder has three prediction heads responsible for reconstructing  $\log(1 + \hat{A})$ ,  $\sin \hat{\phi}$ , and  $\cos \hat{\phi}$ , respectively.

Naively treating the sine and cosine components independently by applying mean squared error to each dimension separately during training fails to explicitly capture the circular nature of phase: minimizing the MSE of sine and cosine individually does not guarantee that the resulting vector lies on the unit circle and it may allow predictions that deviate from valid phase angles. To address these limitations, we introduce a unit circle phase-aware loss  $\mathcal{L}_{\text{unit-loss}}$  that directly optimizes the directional alignment of the predicted phase vector with the target phase while enforcing unit-norm constraints. Specifically, we represent each phase as a 2D vector  $(\cos \phi, \sin \phi)$  and compute the cosine similarity between the predicted and target vectors, combined with a small regularization term that penalizes deviations from unit length:

$$\begin{aligned} \mathcal{L}_{\text{unit-loss}} = & 1 - \sum_i \underbrace{\frac{\cos \hat{\phi}_i \cos \phi_i + \sin \hat{\phi}_i \sin \phi_i}{\sqrt{\cos^2 \hat{\phi}_i + \sin^2 \hat{\phi}_i} \sqrt{\cos^2 \phi_i + \sin^2 \phi_i}}}_{\text{Cosine Similarity}} \\ & + \lambda_{\text{circle}} \cdot \underbrace{\sum_i (\cos^2 \hat{\phi}_i + \sin^2 \hat{\phi}_i - 1)^2}_{\text{Unit-Circle Penalization Term}} \end{aligned} \quad (6)$$

This formulation has several advantages: it naturally respects the circular topology of phase, avoids discontinuities near angular boundaries and ensures that all predicted vectors correspond to valid phase angles. The phases are essentially represented as unit vectors in 2D space, making the errors between them more geometrically meaningful. Finally, although reconstructing raw EEG waveforms is unstable, we found that incorporating a temporal-domain reconstruction

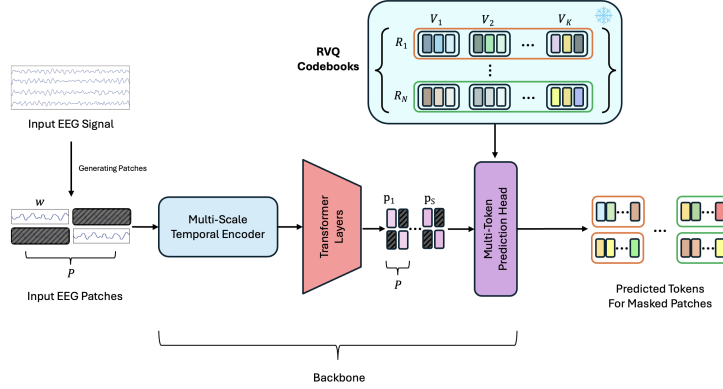


Figure 3. NEURORVQ Foundation Model. During pre-training, random EEG patches are masked, and the model is trained to reconstruct the missing tokens from the RVQ codebook using the surrounding visible patches as context.

loss provides additional guidance. Specifically, we transform the predicted log-amplitude and phase back to the time domain (the predicted log-amplitudes are exponentiated and rescaled to recover the original amplitude spectrum before the inverse Fourier transformation) and compute a temporal MSE regularization term. The NEURORVQ tokenizer is thus trained end-to-end with the objective:

$$\begin{aligned} \mathcal{L}_T = & \sum_i \underbrace{\left\| \log(1 + \hat{A}_i) - \log(1 + A_i) \right\|_2^2}_{\text{Log-Amplitude Loss}} \\ & + \underbrace{\left\| \hat{X}_i - X_i \right\|_2^2}_{\text{Temporal Loss}} + \mathcal{L}_{\text{unit-loss}} + \mathcal{L}_Q \end{aligned} \quad (7)$$

where  $\hat{A}$ ,  $\sin \hat{\phi}$ , and  $\cos \hat{\phi}$  denote reconstructed Fourier components,  $\hat{X}$  denotes reconstructed EEG in the time domain and  $\mathcal{L}_Q$  is the commitment loss.

## 4. NeuroRVQ Foundation Model

NEURORVQ is a scalable foundation model that operates on the tokenized representation. By working at the token level rather than raw signals, this model can better capture long-range dependencies, learn abstract neural dynamics and enable efficient pretraining across diverse EEG datasets. The model leverages the learned codebooks  $\mathcal{R}$  from the tokenizer stage and is trained using a masked-token prediction strategy, where a subset of input patches is randomly masked. This objective encourages the network to infer missing tokens from their surrounding context.

Figure 3 shows the architecture of NEURORVQ foundation model. The architecture consists of a multi-scale temporal encoder (Section 3.1) that extracts hierarchical temporal features across multiple resolutions, followed by a series of transformer layers that model long-range complex de-

pendencies. A series of token prediction heads reconstructs the masked tokens from the contextualized embeddings using the trained  $\mathcal{R}$  codebooks, which are used only during the pre-training of the backbone model. In line with LaBraM (Jiang et al., 2024), a symmetric masking strategy is employed, generating the spatially inverse of each original mask during training to enhance efficiency and data diversity. By combining hierarchical temporal encoding, transformer-based context modeling and symmetric masking, the foundation model effectively captures rich spatio-temporal patterns and produces high-fidelity token predictions. For downstream tasks, the pre-trained backbone is extended with task-specific classifications heads.

## 5. Experiments

We evaluate NEURORVQ along two dimensions: (i) the quality of its tokenizer, compared with the tokenizers of LaBraM (Jiang et al., 2024) and BrainOmni (Xiao et al., 2025), recent state-of-the-art codebook-based methods for signal reconstruction; and (ii) the performance of the NEURORVQ foundation model, compared with other pre-trained open-source models, fine-tuned for downstream tasks.

### 5.1. Experimental Setup

**Hyperparameters / Training Process:** NEURORVQ was trained using the settings described in Appendix B. The tokenizer was trained for 100 epochs with  $S = 4$  temporal branches (selected heuristically based on neuroscientific findings (Newson & Thiagarajan, 2018) - the smallest number that still enables effective disentanglement of the canonical EEG frequency bands) and 4  $\mathcal{R}$  RVQ codebooks each consisting of 8 single codebooks  $\mathcal{V}_i \in \mathbb{R}^{8192 \times 128}$  (see Appendix C) and  $\lambda_{\text{circle}} = 0.4$ . The foundation model was trained for 50 epochs in the same datasets. The experiments were run on NVIDIA DGX with 4 Tesla V100 GPUs.

Table 1. In-distribution validation and out-of-distribution mean squared error (MSE) reconstruction performance across frequency bands for NEURORVQ and LaBraM tokenizers (original pre-trained and ours).

	In-Distribution	Out-of-Dist. (Task)	Raw Signal	Delta	Theta	Alpha	Beta	Gamma
LaBraM (ours)	✓		1.071	1.561	0.184	0.099	0.122	0.020
NEURORVQ	✓		<b>0.016</b>	<b>0.006</b>	<b>0.002</b>	<b>0.002</b>	<b>0.005</b>	<b>0.002</b>
LaBraM (orig.)		✓ - (Memory)	1.985	1.093	0.216	0.191	0.211	0.054
LaBraM (ours)		✓ - (Memory)	1.880	2.757	0.361	0.352	0.161	0.031
NEURORVQ		✓ - (Memory)	<b>0.084</b>	<b>0.046</b>	<b>0.006</b>	<b>0.009</b>	<b>0.022</b>	<b>0.010</b>
LaBraM (orig.)		✓ - (Motor)	2.004	0.863	0.326	0.400	0.350	0.064
LaBraM (ours)		✓ - (Motor)	1.893	3.313	0.669	0.721	0.339	0.049
NEURORVQ		✓ - (Motor)	<b>0.090</b>	<b>0.032</b>	<b>0.010</b>	<b>0.017</b>	<b>0.038</b>	<b>0.009</b>

**Datasets:** We have used 13 large-scale EEG datasets, consisting of 12 public datasets and 1 self-collected motor dataset (we refer the reader to Appendix D). All datasets were resampled to the same sampling frequency of 200Hz.

## 5.2. Tokenizer Evaluation

We compare signal reconstruction errors at a per-patch level of NEURORVQ’s tokenizer with LaBraM (Jiang et al., 2024) (in- and out-of-distribution settings) and BrainOmni (Xiao et al., 2025) (out-of-distribution setting).

### 5.2.1. IN-DISTRIBUTION EVALUATION

To ensure a fair comparison and to properly evaluate the in-distribution reconstruction capabilities, both LaBraM and NEURORVQ were trained on **the same datasets**, with the **same train-validation split**, and **identical training regime**, as described in Section 5.1 (see Appendix E for the learning curves). Figure 4 illustrates the reconstruction of a single EEG signal/patch using the LaBraM and NEURORVQ tokenizers. Table 1 reports the overall reconstruction performance in the validation set across frequency bands. Across all bands, NEURORVQ achieves orders-of-magnitude lower reconstruction error compared to LaBraM, demonstrating that NEURORVQ can produce faithful and robust representations of EEG signals across both broadband and band-specific components.

### 5.2.2. OUT-OF-DISTRIBUTION EVALUATION

We further evaluated the generalization capabilities of both NEURORVQ and LaBraM in reconstructing EEG signals in two datasets unseen during training: a motor dataset High Gamma (Schirrmeister et al., 2017) and a working memory dataset (Pavlov et al., 2022). For LaBraM, we used two variations: (i) the version trained with the same datasets as NEURORVQ, highlighted as *ours*; and (ii) the authors’ pre-trained model, highlighted as *original*. For each dataset, input patches were extracted using the class-related parts of

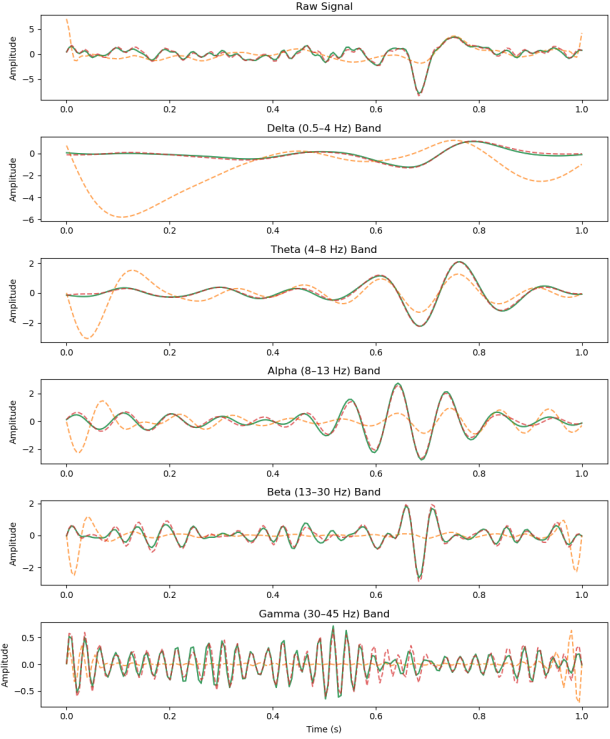


Figure 4. Per-band analysis of a sample reconstructed EEG signal (from the validation set) from LaBraM and NEURORVQ codebook-based tokenizers. Green lines denote the input EEG signal, orange the reconstructed EEG signal for LaBraM (ours) and red the reconstructed EEG signal for NEURORVQ.

each trial in the dataset. Tables 1 show that NEURORVQ consistently outperforms both variations of LaBraM across all frequency bands, demonstrating the robustness and superior generalization of NEURORVQ, even when evaluated on EEG signals from entirely unseen datasets.

While LaBraM’s codebook is inspired by VQ-VAE (Esser et al., 2020), BrainOmni adopts a single RVQ codebook discretization inspired by EnCodec (Défossez et al., 2023). NEURORVQ is also RVQ-based, but differs fundamentally

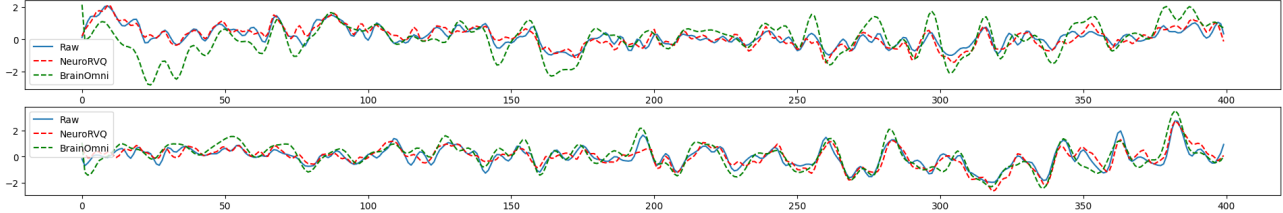


Figure 5. Two sample reconstructed EEG signals from BrainOmni and NEURORVQ codebook-based tokenizers. Blue lines denote the input EEG signal, green the reconstructed EEG signal for BrainOmni and red the reconstructed EEG signal for NEURORVQ.

Table 2. Comparison of classification balanced accuracy between NEURORVQ and other LBMs, finetuned on the same datasets using identical training settings (\* denotes early stopping). Bold and underlined values indicate best performance and next-best performance respectively (per task or overall). Tasks follow the (Lee et al., 2025) benchmark for EEG foundation models.

Model	Motor	ERP	Memory	Sleep*	Eyes	Mean
NeuroGPT	<b><math>0.682 \pm 0.083</math></b>	$0.757 \pm 0.048$	<b><math>0.597 \pm 0.029</math></b>	$0.674 \pm 0.033$	$0.827 \pm 0.036$	$0.707 \pm 0.046$
CBraMod	$0.614 \pm 0.104$	$0.777 \pm 0.052$	$0.574 \pm 0.038$	$0.635 \pm 0.041$	$0.839 \pm 0.041$	$0.688 \pm 0.055$
BIOT	$0.443 \pm 0.079$	$0.500 \pm 0.000$	$0.510 \pm 0.018$	—	$0.763 \pm 0.049$	—
MIRepNet	$0.689 \pm 0.086$	—	—	—	—	—
LaBraM	$0.630 \pm 0.076$	$0.822 \pm 0.040$	$0.526 \pm 0.026$	$0.652 \pm 0.037$	$0.799 \pm 0.047$	$0.686 \pm 0.045$
EEGPT	$0.313 \pm 0.035$	$0.668 \pm 0.146$	$0.520 \pm 0.017$	$0.634 \pm 0.044$	$0.797 \pm 0.037$	$0.587 \pm 0.056$
NEURORVQ	<b><math>0.700 \pm 0.073</math></b>	<b><math>0.876 \pm 0.033</math></b>	$0.574 \pm 0.027$	<b><math>0.728 \pm 0.028</math></b>	<b><math>0.869 \pm 0.026</math></b>	<b><math>0.749 \pm 0.037</math></b>

in that we employ multiple (per frequency scale) RVQ codebooks, rather than a single RVQ. We compare the reconstruction generalization capabilities of NEURORVQ with BrainOmni. We use BrainOmni’s sample data (band-pass filtered between 0.5 and 45Hz) because their model requires device layout information. Since the two architectures employ different signal normalization strategies, we compare them using both strategies to ensure fairness. Table 3 and Figure 5 show that NEURORVQ consistently outperforms BrainOmni in both normalization schemes.

Table 3. Out-of-distribution mean squared error (MSE) reconstruction performance for NEURORVQ and BrainOmni tokenizers with both normalization (Norm) schemes in BrainOmni’s sample data.

	NEURORVQ-Norm.	BO-Norm.
BrainOmni (BO)	0.450	0.332
NEURORVQ	<b>0.191</b>	<b>0.275</b>

### 5.3. Downstream Performance

We evaluated the downstream task performance of finetuned NEURORVQ in comparison to other fine-tuned LBMs, namely NeuroGPT (Cui et al., 2024), CBraMod (Wang et al., 2025), LaBraM (Jiang et al., 2024), EEGPT (Wang et al., 2024), BIOT (Yang et al., 2023)<sup>1</sup> and MIRepNet (Liu et al., 2025)<sup>2</sup>. All models were evaluated in five downstream

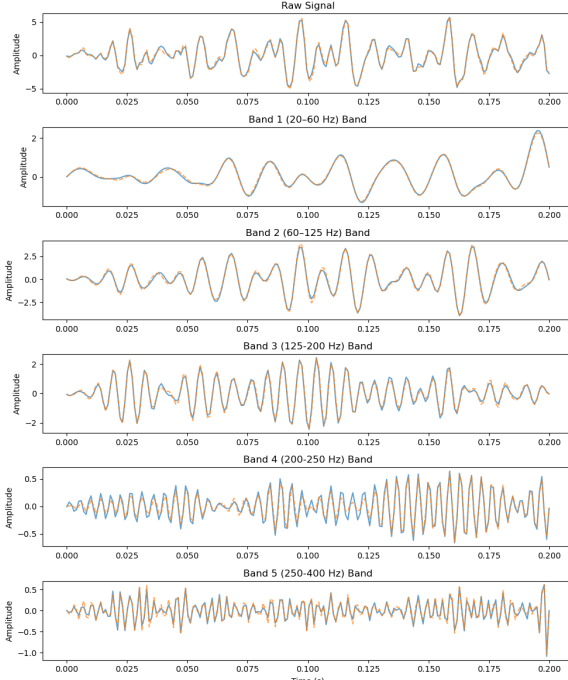
<sup>1</sup>BIOT could not be tested on the Sleep task since the benchmark electrodes are missing from the pre-trained model.

<sup>2</sup>As a motor-related foundation model, MIRepNet was tested only on the motor task

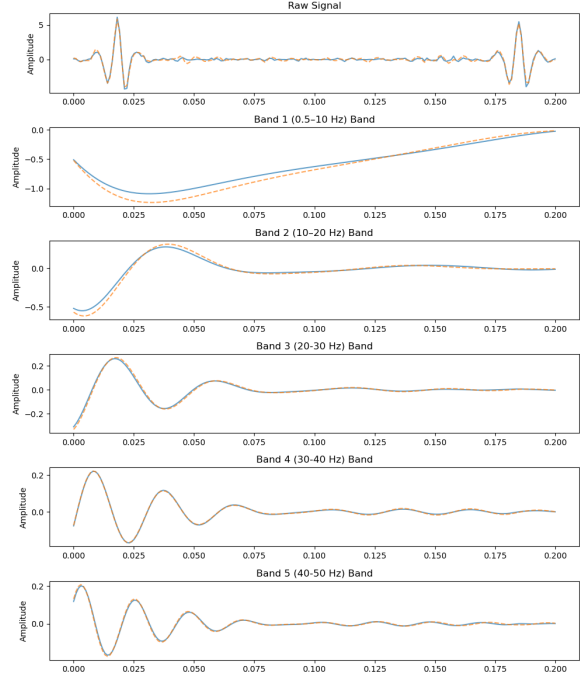
classification tasks (Lee et al., 2025): (a) Motor, a four-class movement classification on High Gamma (Schirrmeister et al., 2017) dataset (14 subjects); (b) ERP (Event-Related Potential), a two-class ERP classification on the ERP paradigm from Korean University (Kim et al., 2019) dataset (54 subjects); (c) Memory, a binary working memory classification on (Pavlov et al., 2022) (65 subjects); (d) Sleep, a 6-class sleep stage classification on Physionet’s Sleep-EDF (Kemp et al., 2000) (78 subjects); and (e) Eyes, eyes open vs. closed classification on Physionet’s Motor (Schalk et al., 2004) (103 subjects). This benchmark (Lee et al., 2025) was selected because its tasks capture a diverse range of BCI paradigms with datasets specifically chosen for their minimal spurious artifacts, reducing the likelihood of spurious performance during training.

We applied the same full fine-tuning procedure to all models, training for 20 epochs since performance plateaued beyond that point. For the sleep task, however, we employed early stopping, as the models began to overfit before reaching 20 epochs. For evaluation, we used a consistent 10-fold subject-independent cross-validation across all models and reported balanced accuracy for each task (for downstream performance comparison between codebook-based LBMs—namely, LaBraM and NEURORVQ—pre-trained on the same datasets see Appendix F). The variance between folds is also reported to highlight model’s robustness.

Table 2 shows that, when full-finetuned, NEURORVQ achieves the best or next-best performance in each task, and the best overall performance, measured as the mean balanced accuracy across all tasks. NEURORVQ has 5.9M



(a) EMG Modality



(b) ECG Modality

Figure 6. Reconstructed sample biosignals (from the validation sets) from NEURORVQ codebook-based tokenizer. Blue lines denote the input biosignal and orange the reconstructed biosignal for NEURORVQ.

parameters in the backbone model and approximately 3K parameters in the classification heads. Yet, it achieves higher mean performance than NeuroGPT, which has 79.5M parameters in its backbone; and it also outperforms CBraMod, which has similar backbone parameters to NEURORVQ but much larger classification heads, approximately 50M parameters (see Appendix G for a detailed comparison of classification head sizes). This combination of strong generalization and compact size highlights the effectiveness of NEURORVQ’s tokenizer.

## 6. Discussion

The NEURORVQ tokenizer demonstrates state-of-the-art reconstruction capabilities on both in- and out-of-distribution signals (Section 5.2). Importantly, these results cannot be attributed solely to the number of codebooks (single or multiple), their size or their type (e.g., RVQ-based). Instead, they arise from the inductive biases embedded in the tokenizer design which, together with the newly introduced unit circle phase-aware training loss, are particularly well-suited for capturing the complex nature of EEG signals.

The main contribution of this work is the NEURORVQ codebook, which can be (i) applied to biosignal modalities beyond EEG and (ii) integrated into larger LBM architectures, enabling further performance improvements.

**Beyond EEG**, the NEURORVQ tokenizer is readily adaptable to other biosignal modalities by adjusting the kernel sizes to capture modality-specific frequency ranges and by scaling the number of RVQ codebooks to model signals of varying complexity. Initial results on EMG and ECG (Appendix H) demonstrate strong reconstruction performance, as illustrated in Figures 6a and 6b respectively. **Further improvements** can come from larger LBM architectures and incorporating causal reasoning-inspired training principles, such as more targeted temporal and spatial masking strategies (Barmpas et al., 2024a). These directions are beyond the scope of this work and promising for future research.

## 7. Conclusion

In this work, we introduce NEURORVQ, an LBM that leverages an RVQ codebook-based tokenizer. Our main contribution is the design and training of the tokenizer, which captures low- and high-frequency components of EEG signals, achieves state-of-the-art reconstruction performance and facilitates the development of more effective LBMs. We further showed that NEURORVQ outperforms existing pre-trained LBMs in various downstream tasks. In summary, NEURORVQ advances the development of efficient LBMs by providing a high-fidelity tokenizer, while its principles can be extended to other biosignals, paving the way for broader use of foundation models in the biosignal space.

## Impact Statement

This paper presents work whose goal is to advance the field of Machine Learning. There are many potential societal consequences of our work, none of which we feel must be specifically highlighted here.

## References

Alkawadri, R. Brain–Computer Interface (BCI) Applications in Mapping of Epileptic Brain Networks Based on Intracranial-EEG: An Update. *Frontiers in Neuroscience*, 13:191, 2019. ISSN 1662-453X. doi: 10.3389/fnins.2019.00191.

Bakas, S., Ludwig, S., Barmpas, K., Bahri, M., Panagakis, Y., Laskaris, N., Adamos, D. A., and Zafeiriou, S. Team Cogitat at NeurIPS 2021: Benchmarks for EEG Transfer Learning Competition, 2022.

Barmpas, K., Panagakis, Y., Adamos, D. A., Laskaris, N., and Zafeiriou, S. BrainWave-Scattering Net: a lightweight network for EEG-based motor imagery recognition. *Journal of Neural Engineering*, 20(5):056014, September 2023. ISSN 1741-2552. doi: 10.1088/1741-2552/acf78a.

Barmpas, K., Panagakis, Y., Adamos, D., Laskaris, N., and Zafeiriou, S. A Causal Perspective in Brainwave Foundation Models. In *Causality and Large Models @NeurIPS 2024*, 2024a. doi: 10.1088/1741-2552/ad3eb5.

Barmpas, K., Panagakis, Y., Zoumpourlis, G., Adamos, D. A., Laskaris, N., and Zafeiriou, S. A causal perspective on brainwave modeling for brain–computer interfaces. *Journal of Neural Engineering*, 21(3):036001, may 2024b. doi: 10.1088/1741-2552/ad3eb5.

Bashashati, A., Fatourechi, M., Ward, R. K., and Birch, G. E. A survey of signal processing algorithms in brain–computer interfaces based on electrical brain signals. *Journal of Neural Engineering*, 4(2):R32–R57, mar 2007. doi: 10.1088/1741-2550/4/2/r03.

Blankertz, B., Dornhege, G., Krauledat, M., Müller, K.-R., and Curio, G. The non-invasive Berlin Brain–Computer Interface: Fast acquisition of effective performance in untrained subjects. *NeuroImage*, 37(2):539–550, 2007. ISSN 1053-8119. doi: <https://doi.org/10.1016/j.neuroimage.2007.01.051>.

Brown, T. B., Mann, B., Ryder, N., Subbiah, M., Kaplan, J., Dhariwal, P., Neelakantan, A., Shyam, P., Sastry, G., Askell, A., Agarwal, S., Herbert-Voss, A., Krueger, G., Henighan, T., Child, R., Ramesh, A., Ziegler, D. M., Wu, J., Winter, C., Hesse, C., Chen, M., Sigler, E., Litwin, M., Gray, S., Chess, B., Clark, J., Berner, C., McCandlish, S., Radford, A., Sutskever, I., and Amodei, D. Language Models are Few-Shot Learners, 2020.

Buckwalter, G., Chhin, S., Rahman, S., Obeid, I., and Picone, J. Recent Advances in the TUH EEG Corpus: Improving the Interrater Agreement for Artifacts and Epileptiform Events. In *2021 IEEE Signal Processing in Medicine and Biology Symposium (SPMB)*, pp. 1–3, 2021. doi: 10.1109/SPMB52430.2021.9672302.

Cui, W., Jeong, W., Thölke, P., Medani, T., Jerbi, K., Joshi, A. A., and Leahy, R. M. Neuro-GPT: Towards A Foundation Model for EEG, 2024.

Défosssez, A., Copet, J., Synnaeve, G., and Adi, Y. High fidelity neural audio compression. *Transactions on Machine Learning Research*, 2023. ISSN 2835-8856. Featured Certification, Reproducibility Certification.

Dehghani, M., Djolonga, J., Mustafa, B., Padlewski, P., Heek, J., Gilmer, J., Steiner, A., Caron, M., Geirhos, R., Alabdulmohsin, I., Jenatton, R., Beyer, L., Tschannen, M., Arnab, A., Wang, X., Riquelme, C., Minderer, M., Puigcerver, J., Evci, U., Kumar, M., van Steenkiste, S., Elsayed, G. F., Mahendran, A., Yu, F., Oliver, A., Huot, F., Bastings, J., Collier, M. P., Gritsenko, A., Birodkar, V., Vasconcelos, C., Tay, Y., Mensink, T., Kolesnikov, A., Pavetić, F., Tran, D., Kipf, T., Lučić, M., Zhai, X., Keysers, D., Harmsen, J., and Houlsby, N. Scaling Vision Transformers to 22 Billion Parameters, 2023.

Detti, P., Vatti, G., and Zabalo Manrique de Lara, G. EEG Synchronization Analysis for Seizure Prediction: A Study on Data of Noninvasive Recordings. *Processes*, 8:846, 07 2020. doi: 10.3390/pr8070846.

Djoufack Nkengfack, L. C., Tchiotsop, D., Atangana, R., Louis-Door, V., and Wolf, D. Classification of EEG signals for epileptic seizures detection and eye states identification using Jacobi polynomial transforms-based measures of complexity and least-square support vector machine. *Informatics in Medicine Unlocked*, 23:100536, 2021. ISSN 2352-9148. doi: 10.1016/j.imu.2021.100536.

Esser, P., Rombach, R., and Ommer, B. Taming Transformers for High-Resolution Image Synthesis, 2020.

Gray, R. M. Vector quantization. *IEEE ASSP Magazine*, 1: 4–29, 1984.

Handy, T. C. *Brain Signal Analysis: Advances in Neuroelectric and Neuromagnetic Methods*. The MIT Press, 07 2009. ISBN 9780262013086. doi: 10.7551/mitpress/9780262013086.001.0001.

Irimia, D., Ortner, R., Krausz, G., Guger, C., and Pobornicu, M. BCI Application in Robotics Control. *IFAC Proceedings Volumes*, 45(6):1869–1874, 2012. ISSN

1474-6670. doi: 10.3182/20120523-3-RO-2023.00432. 14th IFAC Symposium on Information Control Problems in Manufacturing.

Jiang, W., Zhao, L., and liang Lu, B. Large brain model for learning generic representations with tremendous EEG data in BCI. In *The Twelfth International Conference on Learning Representations*, 2024.

Kemp, B., Zwinderman, A. H., Tuk, B., Kamphuisen, H. A. C., and Obreyé, J. J. L. Analysis of a sleep-dependent neuronal feedback loop: the slow-wave microcontinuity of the EEG. *IEEE Transactions on Biomedical Engineering*, 47(9):1185–1194, 2000. doi: 10.1109/10.867928.

Kim, H.-K., Williamson, J., Lee, M.-H., Kwon, O.-Y., Lee, S.-W., Fazli, S., Kim, Y.-J., and Lee, Y.-E. Supporting data for "EEG Dataset and OpenBMI Toolbox for Three BCI Paradigms: An Investigation into BCI Illiteracy", 2019.

Korczowski, L., Cederhout, M., Andreev, A., Cattan, G., Rodrigues, P., Gautheret, V., and Congedo, M. Brain Invaders calibration-less P300-based BCI with modulation of flash duration Dataset (bi2015a), 07 2019.

Lawhern, V. J., Solon, A. J., Waytowich, N. R., Gordon, S. M., Hung, C. P., and Lance, B. J. EEGNet: A Compact Convolutional Neural Network for EEG-based Brain–Computer Interfaces. *Journal of Neural Engineering*, 15(5):056013, July 2018. ISSN 1741-2552. doi: 10.1088/1741-2552/aace8c.

Lee, N., Bakas, S., Barmpas, K., Panagakis, Y., Adamos, D., Laskaris, N., and Zafeiriou, S. Assessing the capabilities of large brainwave foundation models. In *2025 IEEE 35th International Workshop on Machine Learning for Signal Processing (MLSP)*, pp. 01–06, 2025. doi: 10.1109/MLSP62443.2025.11204282.

Liu, D., Chen, Z., Luo, J., Lian, S., and Wu, D. Mirepnet: A pipeline and foundation model for eeg-based motor imagery classification, 2025.

Luciw, M., Jarocka, E., and Edin, B. Multi-channel EEG recordings during 3,936 grasp and lift trials with varying weight and friction. *Scientific data*, 1:140047, 11 2014. doi: 10.1038/sdata.2014.47.

Margaux, P., Maby, E., Daligault, S., Bertrand, O., and Mattout, J. Objective and Subjective Evaluation of Online Error Correction during P300-Based Spelling. *Advances in Human-Computer Interaction*, 2012, 01 2012. doi: 10.1155/2012/578295.

McFarland, D. J., Anderson, C. W., Müller, K.-R., Schlögl, A., and Krusienski, D. J. BCI meeting 2005-workshop on BCI signal processing: feature extraction and translation. *IEEE Transactions on Neural Systems and Rehabilitation Engineering*, 14(2):135–138, 2006. doi: 10.1109/TNSRE.2006.875637.

Mizrahi, D., Bachmann, R., Kar, O. F., Yeo, T., Gao, M., Dehghan, A., and Zamir, A. 4M: Massively Multimodal Masked Modeling. In *Thirty-seventh Conference on Neural Information Processing Systems*, 2023.

Nam, C., Nijholt, A., and Lotte, F. (eds.). *Brain-Computer Interfaces Handbook: Technological and Theoretical Advances*. CRC Press (Taylor & Francis), January 2018. ISBN 9781498773430.

Newson, J. J. and Thiagarajan, T. C. EEG frequency bands in psychiatric disorders: A review of resting state studies. *Front. Hum. Neurosci.*, 12:521, 2018.

Pavlov, Y. G., Kasanov, D., Kosachenko, A. I., and Kotyusov, A. I. "EEG, pupillometry, ECG and photoplethysmography, and behavioral data in the digit span task and rest", 2022.

Rao, R. P. *Brain-Computer Interfacing: An Introduction*. Cambridge University Press, USA, 2013. ISBN 0521769418.

Salter, S., Warren, R., Schlager, C., Spurr, A., Han, S., Bhasin, R., Cai, Y., Walkington, P., Bolarinwa, A., Wang, R., et al. emg2pose: A large and diverse benchmark for surface electromyographic hand pose estimation. In *The Thirty-eight Conference on Neural Information Processing Systems Datasets and Benchmarks Track*, 2024.

Santamaría-Vázquez, E., Martínez-Cagigal, V., Vaquerizo-Villar, F., and Hornero, R. EEG-Inception: A Novel Deep Convolutional Neural Network for Assistive ERP-Based Brain-Computer Interfaces. *IEEE Transactions on Neural Systems and Rehabilitation Engineering*, 28(12): 2773–2782, 2020. doi: 10.1109/TNSRE.2020.3048106.

Schalk, G., McFarland, D. J., Hinterberger, T., Birbaumer, N., and Wolpaw, J. R. BCI2000: a general-purpose brain-computer interface (BCI) system. *IEEE Trans. Biomed. Eng.*, 51(6):1034–1043, June 2004. doi: 10.1109/TBME.2004.827072.

Schirrmeister, R. T., Springenberg, J. T., Fiederer, L. D. J., Glasstetter, M., Eggensperger, K., Tangermann, M., Hutter, F., Burgard, W., and Ball, T. Deep learning with convolutional neural networks for EEG decoding and visualization. *Human brain mapping*, 38(11):5391–5420, 2017.

Shah, V., von Weltin, E., López, S., McHugh, J. R., Veloso, L., Golmohammadi, M., Obeid, I., and Picone, J. The Temple University Hospital Seizure Detection Corpus, 2018.

Song, Y., Zheng, Q., Liu, B., and Gao, X. EEG Conformer: Convolutional Transformer for EEG Decoding and Visualization. *IEEE Transactions on Neural Systems and Rehabilitation Engineering*, 31:710–719, 2023. doi: 10.1109/TNSRE.2022.3230250.

Torkamani-Azar, M., Kanik, S. D., Aydin, S., and Cetin, M. Prediction of Reaction Time and Vigilance Variability from Spatirospectral Features of Resting-State EEG in a Long Sustained Attention Task, 2019.

Torres, E. P., Torres, E. A., Hernández-Álvarez, M., and Yoo, S. G. EEG-Based BCI Emotion Recognition: A Survey. *Sensors*, 20(18), 2020. ISSN 1424-8220. doi: 10.3390/s20185083.

Touvron, H., Lavril, T., Izacard, G., Martinet, X., Lachaux, M.-A., Lacroix, T., Rozière, B., Goyal, N., Hambro, E., Azhar, F., Rodriguez, A., Joulin, A., Grave, E., and Lample, G. LLaMA: Open and Efficient Foundation Language Models, 2023.

Trujillo, L. Raw EEG Data, 2020.

Trujillo, L. T., Stanfield, C. T., and Vela, R. D. The Effect of Electroencephalogram (EEG) Reference Choice on Information-Theoretic Measures of the Complexity and Integration of EEG Signals. *Frontiers in Neuroscience*, Volume 11 - 2017, 2017. ISSN 1662-453X. doi: 10.3389/fnins.2017.00425.

Vaswani, A., Shazeer, N., Parmar, N., Uszkoreit, J., Jones, L., Gomez, A. N., Kaiser, L., and Polosukhin, I. Attention Is All You Need, 2023.

Veloso, L., McHugh, J. R., von Weltin, E., López, S., Obeid, I., and Picone, J. Big data resources for EEGs: Enabling deep learning research. In *2017 IEEE Signal Processing in Medicine and Biology Symposium (SPMB)*, pp. 1–3, 2017. doi: 10.1109/SPMB.2017.8257044.

Wagner, P., Strothoff, N., Bousseljot, R.-D., Samek, W., and Schaeffter, T. PTB-XL, a large publicly available electrocardiography dataset, 2022.

Wang, G., Liu, W., He, Y., Xu, C., Ma, L., and Li, H. EEGPT: Pretrained Transformer for Universal and Reliable Representation of EEG Signals. In *The Thirty-eighth Annual Conference on Neural Information Processing Systems*, 2024.

Wang, J., Zhao, S., Luo, Z., Zhou, Y., Jiang, H., Li, S., Li, T., and Pan, G. CBraMod: A Criss-Cross Brain Foundation Model for EEG Decoding. In *The Thirteenth International Conference on Learning Representations*, 2025. doi: 10.48550/arXiv.2412.07236.

Wei, X., Faisal, A. A., Grosse-Wentrup, M., Gramfort, A., Chevallier, S., Jayaram, V., Camille Jeunet, S. B., Ludwig, S., Barmpas, K., Bahri, M., Panagakis, Y., Laskaris, N., Adamos, D. A., Zafeiriou, S., Duong, W. C., Gordon, S. M., Lawhern, V. J., Śliwowski, M., Rouanne, V., and Tempczyk, P. 2021 BEETL Competition: Advancing Transfer Learning for Subject Independence & Heterogeneous EEG Data Sets, 2022.

Xiao, Q., Cui, Z., Zhang, C., Chen, S., Wu, W., Thwaites, A., Woolgar, A., Zhou, B., and Zhang, C. Brainomni: A brain foundation model for unified EEG and MEG signals. In *The Thirty-ninth Annual Conference on Neural Information Processing Systems*, 2025.

Xu, T., Zhou, Y., Wang, Z., and Peng, Y. Learning Emotions EEG-based Recognition and Brain Activity: A Survey Study on BCI for Intelligent Tutoring System. *Procedia Computer Science*, 130:376–382, 2018. ISSN 1877-0509. doi: j.procs.2018.04.056. The 9th International Conference on Ambient Systems, Networks and Technologies (ANT 2018) / The 8th International Conference on Sustainable Energy Information Technology (SEIT-2018) / Affiliated Workshops.

Yang, C., Westover, M., and Sun, J. BIOT: Biosignal Transformer for Cross-data Learning in the Wild. In Oh, A., Naumann, T., Globerson, A., Saenko, K., Hardt, M., and Levine, S. (eds.), *Advances in Neural Information Processing Systems*, volume 36, pp. 78240–78260. Curran Associates, Inc., 2023.

## A. Sine-Cosine Phase Representation

We describe the benefits of using a sine-cosine representation of the Fourier phase  $\phi$  in the loss function, instead of the raw phase values.

LaBraM (Jiang et al., 2024) computes phase loss directly as the squared error between predicted  $\hat{\phi}$  and true  $\phi$ :

$$\mathcal{L}_\phi = \|\hat{\phi} - \phi\|^2. \quad (8)$$

This formulation, however, is discontinuous at the boundaries of the phase domain  $[-\pi, \pi]$ . For instance, with  $\hat{\phi} = \pi - \epsilon$  and  $\phi = -\pi + \epsilon$  for small  $\epsilon > 0$ ,

$$\mathcal{L}_\phi = \|\hat{\phi} - \phi\|^2 = (2\pi - 2\epsilon)^2. \quad (9)$$

The loss approaches  $4\pi^2$ , even though the two angles are nearly identical. Thus, small phase shifts near the  $\pm\pi$  boundary (e.g.,  $2^\circ$  between  $179^\circ$  and  $-179^\circ$ ) result in large discontinuous jumps in the loss, leading to unstable gradients and poor convergence.

To address this issue, we map phase  $\phi$  to its sine and cosine components, a point on the unit circle:

$$r(\phi) = (\sin(\phi), \cos(\phi)) \in \mathbb{R}^2, \quad (10)$$

The corresponding loss is:<sup>3</sup>

$$\mathcal{L}_{r(\phi)} = \|\sin(\hat{\phi}) - \sin(\phi)\|^2 + \|\cos(\hat{\phi}) - \cos(\phi)\|^2 = 2 - 2\cos(\hat{\phi} - \phi) \quad (11)$$

Our formulation is continuous across the  $\pm\pi$  boundary. Revisiting the earlier example with  $\hat{\phi} = \pi - \epsilon$  and  $\phi = -\pi + \epsilon$ ,

$$\mathcal{L}_{r(\phi)} = 2 - 2\cos(2\epsilon) \approx 4\epsilon^2 \quad (12)$$

which smoothly approaches 0 as  $\epsilon \rightarrow 0$ .

More generally, for any two phases  $\phi_1$  and  $\phi_2$ :

$$\mathcal{L}_{r(\phi)} = 2 - 2\cos(\phi_1 - \phi_2) = 4\sin^2\left(\frac{\phi_1 - \phi_2}{2}\right). \quad (13)$$

$\mathcal{L}_{r(\phi)}$  is the squared chord length on the unit circle between points at angles  $\phi_1$  and  $\phi_2$ .

## B. Model Configuration & Hyperparameter Settings

This section details: (i) the configuration of NEURORVQ’s multi-scale temporal encoder (§B.1), and (ii) the hyperparameter settings used for training the tokenizer and foundation model, as well as fine-tuning the latter on downstream tasks (§B.2).

### B.1. Multi-Scale Temporal Encoder Architecture

*Table 4.* Configuration of the multi-scale temporal encoder, used identically in both the tokenizer and the foundation model. Here,  $x \rightarrow y$  indicates values for the first ( $x$ ) and second ( $y$ ) sequence.

Branch №	Filters	Kernel	Padding	Pooling
1	$8 \rightarrow 8$	$(1, 21) \rightarrow (1, 9)$	$(0, 10) \rightarrow (0, 4)$	$(1, 2) \rightarrow (1, 4)$
2	$8 \rightarrow 8$	$(1, 15) \rightarrow (1, 7)$	$(0, 7) \rightarrow (0, 3)$	$(1, 2) \rightarrow (1, 4)$
3	$8 \rightarrow 8$	$(1, 9) \rightarrow (1, 5)$	$(0, 4) \rightarrow (0, 2)$	$(1, 2) \rightarrow (1, 4)$
4	$8 \rightarrow 8$	$(1, 5) \rightarrow (1, 3)$	$(0, 2) \rightarrow (0, 1)$	$(1, 2) \rightarrow (1, 4)$

Our temporal encoder comprises four temporal branches. Each branch applies the following sequence of operations twice in succession (Figure 1c): a 1-D convolution, followed by group normalization with  $N = 4$  groups and  $C = 8$  channels, GELU activation, and pooling. Table 4 lists the filter counts, kernel sizes, padding, and pooling parameters for the two sequences, where  $x \rightarrow y$  denotes the configuration value(s) used in the first and second sequence, respectively.

<sup>3</sup>Although the NEURORVQ architecture uses the  $\mathcal{L}_{\text{unit-loss}}$  as described in the manuscript, we use  $\mathcal{L}_{r(\phi)}$  here to illustrate the effectiveness of the sine-cosine representation.

## B.2. Hyperparameter Settings

Table 5. NEURORVQ Hyperparameters

Hyperparameter	Tokenizer	Pre-training FM	Finetuning
Temporal Inception Branches $S$	4	4	4
RVQ Codebook $\mathcal{R}$	4	4	4
Single VQ Codebook $\mathcal{V}_i$	8	8	8
Batch size	256	64	64
Learning rate scheduler	Cosine	Cosine	Linear
Base learning rate	5e-5	5e-4	5e-4
Min learning rate	1e-5	1e-5	-
Warmup lr start-end factors	-	-	(0.1,1)
Lr start-end factors	-	-	(1,0.1)
Total epochs	100	50	20
Warmup epochs	10	5	4
Optimizer	AdamW	AdamW	AdamW
Weight decay	1e-4	0.05	0.01
Adam $\beta$	(0.9, 0.999)	(0.9, 0.999)	(0.9, 0.999)
Layer lr decay	-	-	0.975
Masking Ratio	-	0.5	-
Gradient clipping	3	-	-
Layer scale init	0.001	0.001	-
Encoder depth	12	12	12
Decoder depth	3	-	-
Hidden dimension	200	200	200
No. Attention heads	10	10	10
MLP hidden dimension	800	800	800

Table 5 summarises the hyperparameters used for training the tokenizer and for pre-training and fine-tuning the foundation model. Certain choices (e.g., batch size) were constrained by hardware, while others were guided by ablation studies (e.g., using 8 codebooks per RVQ yielded the lowest reconstruction error; see §C).

## C. Number of Codebooks per RVQ

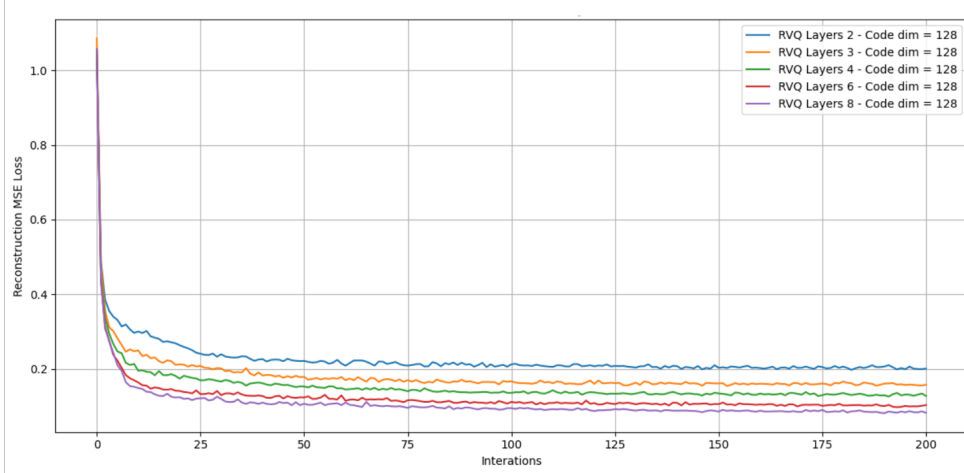


Figure 7. Validation mean squared error (MSE) reconstruction loss for the NEURORVQ tokenizer with different numbers of codebooks (layers) per RVQ codebook.

We conducted an ablation study to determine the best number of codebooks (layers) per RVQ. The tokenizer was trained using our self-collected dataset (see §D), varying the number of layers from 2 to 8. Figure 7 shows that using eight layers  $\mathcal{V}_i \in \mathbb{R}^{8192 \times 128}$  achieve the best reconstruction performance on the validation set.

## D. Datasets

Table 6. Datasets used for pre-training NEURORVQ, with BCI paradigm and number of EEG recording channels.

Datasets	BCI paradigm	# channels
BCI Competition IV-1 (Blankertz et al., 2007)	Motor	64
Grasp and Lift (Luciw et al., 2014)	Motor	32
Physionet MI (Schalk et al., 2004)	Motor	64
bi2015a (Korczowski et al., 2019)	ERP	32
Inria BCI Challenge (Margaux et al., 2012)	ERP	56
Trujillo (2020)	II-RB	64
Trujillo et al. (2017)	Resting	64
SPIS Resting (Torkamani-Azar et al., 2019)	Resting	64
TUAR (Buckwalter et al., 2021)	Artifacts (e.g., eye movement)	31
Siena Scalp (Detti et al., 2020)	Epilepsy	31
TUEP (Veloso et al., 2017)	Epilepsy	31
TUSZ (Shah et al., 2018)	Seizure	31
Self-Collected Dataset	Motor	29

We use a collection of publicly available EEG datasets to pre-train NEURORVQ. Table 6 summarizes the datasets, their associated BCI paradigms, and the number of EEG recording channels. The collection spans multiple experimental settings, including motor imagery, event-related potentials (ERP), resting-state activity, information-integration and rule-based cognitive categorization (II-RB), and clinical data for epilepsy and seizures.

We additionally include a proprietary dataset comprising approximately 235 hours of motor imagery data recorded with 29 channels. Participants in this data collection were instructed as follows:

“We will record your brain waves while you engage in simple tasks. These include real and imagined movements of the extremities, and a game which uses movements as controls. The collected data will be used to train algorithms that can be used for many things, such as facilitating navigation in virtual environments, seamless user interaction with objects in computer gaming or even rehabilitation training of post-stroke patients towards regaining the ability to control their limbs. The project received approval from the Research Governance and Integrity Team. If you want to help out our research team you can register to be a participant in our experiment! There is a small gift of £30 to every participant.”

## E. NEURORVQ vs. LaBraM: Reconstruction Performance

We train NEURORVQ and LaBraM tokenizers on the same datasets with the same train-validation split and an identical training regime (including preprocessing and training steps), as described in §5.1. Figure 8 shows the validation learning curves for both models. NEURORVQ achieves nearly two orders of magnitude lower reconstruction mean squared error (MSE) compared to LaBraM.

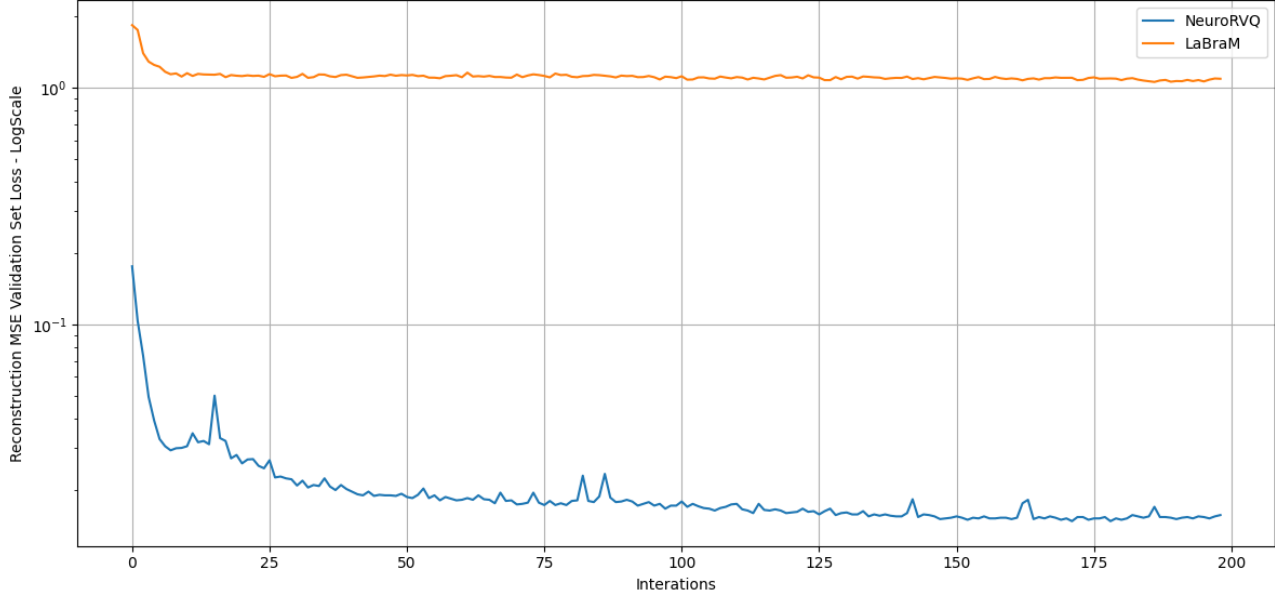


Figure 8. Validation learning curves showing reconstruction mean squared error (MSE) for NEURORVQ and LaBraM tokenizers, trained under identical regimes.

## F. NEURORVQ vs. LaBraM: Downstream Task Performance

We compare the downstream task performance of NEURORVQ with LaBraM when both models are pre-trained and fine-tuned on the same datasets and with an identical training regime. We use a 10-fold subject-independent cross-validation to evaluate models on four classification benchmarks (Motor, Memory, Sleep, Eyes) as described in §5.3. Table 7 shows that, when all training settings are equal, NEURORVQ achieves 1%–13% higher balanced accuracy than LaBraM on all tasks, demonstrating the effectiveness of our tokenizer in training codebook-based models.

Table 7. Comparison of classification balanced accuracy between NEURORVQ and LaBraM, both pre-trained and finetuned on the same datasets using identical settings. (\* denotes early stopping)

Model	Motor	Memory	Sleep*	Eyes
LaBraM (ours)	0.570	0.565	0.715	0.805
NEURORVQ	0.700	0.573	0.728	0.869

## G. Classification Head Sizes

Previously, in Table 2, we compared the downstream classification performance of NEURORVQ against other pre-trained state-of-the-art models: CBraMod, BIOT, EEGPT, NeuroGPT and LaBraM. Here, we report the number of parameters in the task-specific classification head for each model. CBraMod and NeuroGPT employ a 3-layer MLP as their classification heads, according to their original implementations, while the others use a single layer. The head sizes vary with the number of target classes (Motor has 4, ERP has 2, Memory 2, Sleep 6 and Eyes 2); and for CBraMod, also with the number of EEG channels. Table 8 shows that NEURORVQ has a relatively low number of parameters compared to other models, both in the backbone and in the classification heads.

Table 8. Parameter counts for model backbones and task-specific classification heads.

Model	Backbone	Motor Head	ERP Head	Memory Head	Sleep Head	Eyes Head
NeuroGPT	79.5M	270,756	270,657	270,657	270,822	270,657
CBraMod	4.9M	50.1M	40M	40.5M	73M	41M
BIOT	3.2M	1,028	257	257	-	257
LaBraM	5.8M	804	201	201	1,206	201
EEGPT	25.7M	260	65	65	390	65
NEURORVQ	5.9M	3,204	801	801	4,806	801

## H. Tokenization of Biosignal Modalities

The principles underlying NEURORVQ’s tokenizer apply to other biosignals, enabling broader applications of foundation models in the biosignal domain. In this section, we present signal reconstruction results on two additional modalities: electromyography (EMG) and electrocardiogram (ECG).

For ECG, we used the PTB-XL dataset (Wagner et al., 2022), resampled at 200Hz. The NEURORVQ tokenizer was trained using the settings detailed in Appendix B. Training was conducted for 100 epochs with  $S = 4$  temporal branches and 4  $\mathcal{R}$  RVQ codebooks, each consisting of 8 single codebooks  $\mathcal{V}_i \in \mathbb{R}^{8192 \times 128}$ , with 200ms patch time window and  $\lambda_{circle} = 0.4$ . Figure 6b shows the reconstruction of an ECG signal, demonstrating excellent fidelity.

For EMG, we used the emg2pose dataset (Salter et al., 2024), resampled at 1000Hz. The NEURORVQ tokenizer used the same configuration as above, except that each of the 4  $\mathcal{R}$  RVQ codebooks contained 16 single codebooks  $\mathcal{V}_i \in \mathbb{R}^{8192 \times 128}$  (since the complexity of EMG signals and the frequencies of interest are larger than ECG), with 200ms patch time window and  $\lambda_{circle} = 0.4$  and the kernel sizes appropriately adapted as detailed in Table 9. Figure 6a shows the reconstruction of an EMG signal, showing high accuracy in preserving its original features.

Table 9. Configuration of the multi-scale temporal encoder used in the EMG tokenizer. Here,  $x \rightarrow y$  indicates values for the first ( $x$ ) and second ( $y$ ) sequence.

Branch №	Filters	Kernel	Padding	Pooling
1	$8 \rightarrow 8$	$(1, 51) \rightarrow (1, 25)$	$(0, 25) \rightarrow (0, 12)$	$(1, 2) \rightarrow (1, 4)$
2	$8 \rightarrow 8$	$(1, 17) \rightarrow (1, 9)$	$(0, 8) \rightarrow (0, 4)$	$(1, 2) \rightarrow (1, 4)$
3	$8 \rightarrow 8$	$(1, 8) \rightarrow (1, 4)$	$(0, 4) \rightarrow (0, 2)$	$(1, 2) \rightarrow (1, 4)$
4	$8 \rightarrow 8$	$(1, 5) \rightarrow (1, 3)$	$(0, 2) \rightarrow (0, 1)$	$(1, 2) \rightarrow (1, 4)$